

Intermetallic Cobalt Indium Nanoparticles as Oxygen Evolution Reaction Precatalyst: A Non-Leaching p-Block Element

J. Niklas Hausmann, Marten Ashton, Stefan Mebs, Carsten Walter, Sören Selve, Michael Haumann, Tobias Sontheimer, Holger Dau, Matthias Driess, and Prashanth W. Menezes*

Merely all transition-metal-based materials reconstruct into similar oxyhydroxides during the electrocatalytic oxygen evolution reaction (OER), severely limiting the options for a tailored OER catalyst design. In such reconstructions, initial constituent p-block elements take a sacrificial role and leach into the electrolyte as oxyanions, thereby losing the ability to tune the catalyst's properties systematically. From a thermodynamic point of view, indium is expected to behave differently and should remain in the solid phase under alkaline OER conditions. However, the structural behavior of transition metal indium phases during the OER remains unexplored. Herein, are synthesized intermetallic cobalt indium (CoIn_3) nanoparticles and revealed by in situ X-ray absorption spectroscopy and scanning transmission microscopy that they undergo phase segregation to cobalt oxyhydroxide and indium hydroxide. The obtained cobalt oxyhydroxide outperforms a metallic-cobalt-derived one due to more accessible active sites. The observed phase segregation shows that indium behaves distinctively differently from most p-block elements and remains at the electrode surface, where it can form lasting interfaces with the active metal oxo phases.

into chemical energy.^[1] However, these reductive, electrocatalytic half-reactions require an anodic counterpart supplying protons and electrons.^[2] This critical counterpart is the kinetically demanding oxygen evolution reaction (OER).^[2] To improve the overall energy efficiency of these processes, mainly Fe-, Co-, and Ni-based electrocatalysts have been applied for the alkaline OER.^[3] To fine-tune the catalytic properties of the Fe, Co, and Ni active sites, a wide range of composites with p-block elements have been investigated such as chalcogenides,^[4-6] pnictides,^[4,7] phosphates,^[8] borophosphates,^[9,10] borides,^[11] intermetallics,^[12,13] and others.^[14] However, post and in situ characterizations have shown that these materials reconstruct during the strongly oxidizing OER conditions under the formation of p-block element oxyanions and their subsequent leaching into the electrolyte,^[15-18] leaving behind Fe, Co, or Ni oxyhydroxides.^[5,19] This reconstruction

into similar oxyhydroxides strongly limits the design opportunities for OER electrocatalysts.^[15,19]

The observed reconstructions into oxyhydroxides and water-soluble oxyanions align with the Pourbaix diagrams of the respective elements.^[15,20] Unlike all other p-block elements, only In,

1. Introduction

The hydrogen evolution and carbon dioxide reduction reactions are essential to decarbonize the chemical industry and parts of the energy sector, as they can transform carbon-neutral electricity

J. N. Hausmann, C. Walter, P. W. Menezes
Material Chemistry Group for Thin Film Catalysis–CatLab
Helmholtz-Zentrum Berlin für Materialien und Energie
Albert-Einstein-Str. 15, 12489 Berlin, Germany
E-mail: prashanth.menezes@helmholtz-berlin.de

M. Ashton, M. Driess, P. W. Menezes
Department of Chemistry: Metalorganics and Inorganic Materials
Technische Universität Berlin
Straße des 17 Juni 135, Sekr. C2, 10623 Berlin, Germany
S. Mebs, M. Haumann, H. Dau
Department of Physics
Freie Universität Berlin
Arnimallee 14, 14195 Berlin, Germany
S. Selve
Center for Electron Microscopy (ZELMI)
Technische Universität Berlin
Straße des 17. Juni 135, Sekr. KWT2, 10623 Berlin, Germany
T. Sontheimer
Strategy Department of Energy and Information
Helmholtz-Zentrum Berlin für Materialien und Energie
Hahn-Meitner-Platz 1, 14109 Berlin, Germany

 The ORCID identification number(s) for the author(s) of this article can be found under <https://doi.org/10.1002/smll.202309749>

© 2024 The Authors. Small published by Wiley-VCH GmbH. This is an open access article under the terms of the [Creative Commons Attribution License](https://creativecommons.org/licenses/by/4.0/), which permits use, distribution and reproduction in any medium, provided the original work is properly cited.

DOI: 10.1002/smll.202309749

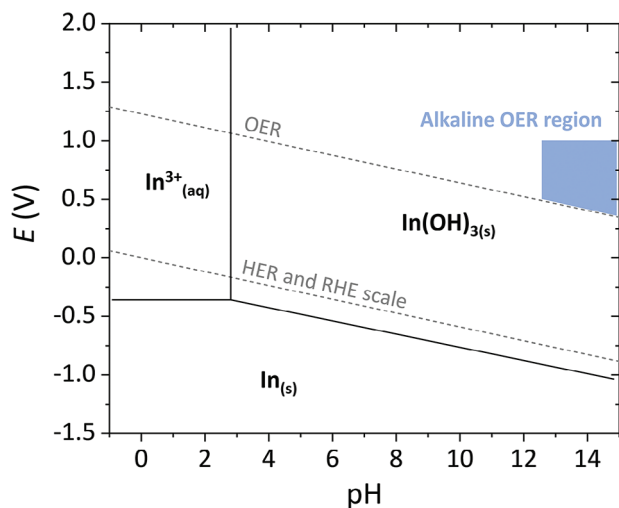


Figure 1. The Pourbaix diagram of indium (25 °C, 0.1 M).^[20] The potential of the x-axis is against the standard hydrogen electrode. In the blue-marked OER region, non-soluble indium hydroxide is the most stable species. For all p-block elements except indium, lead, and bismuth, water-soluble oxyanions are the most stable species in this region.^[15,20]

Pb, and Bi contain non-water-soluble species under alkaline OER conditions (Figure 1 for the Pourbaix diagram of indium).^[15,20] Thus, they should not leach during the OER. This different thermodynamic property could enable the formation of new, stable OER catalysts containing the transition metal and In, Pb, or Bi. To investigate this, we have chosen to synthesize intermetallic cobalt indium (CoIn_3), as indium is the least toxic of all three elements, and the reconstruction of indium-containing transition metal precatalysts has not been investigated so far.^[21–31]

To obtain the desired intermetallic cobalt indium, we developed a reductive wet chemical approach that yields nanoparticles, requires only mild temperatures, and needs only one step. We find that cobalt-indium-derived oxyhydroxides have a higher electrocatalytic OER performance than cobalt-derived ones due to more accessible active sites. In situ and post-catalytic analyses reveal phase segregation of cobalt indium to cobalt oxyhydroxide and indium hydroxide during the OER on the electrode.

2. Results

2.1. As-Prepared Cobalt Indium

Cobalt(II) and indium(III) chloride were reduced with sodium borohydride at 180 °C in tetraethylene glycol and in the presence of a surfactant (see Supporting Information for more details). A ratio of cobalt to indium of 1 to 2.5 was used, as a higher indium ratio led to the formation of crystalline indium. The obtained black powder's X-ray diffraction pattern (XRD) shows exclusively peaks of a CoIn_3 phase (JCPDS 41–880, Figure 2a). The Scherrer equation indicates a crystallite size of around 50 nm (see Supporting Information for details). CoIn_3 is an intermetallic compound wherein cobalt is coordinated by seven indium atoms at 2.60–2.75 Å (Figure 2b). Scanning electron microscopy (SEM) with energy-dispersive X-ray mapping (EDX, Figure 2c–e and Figure S1, Supporting Information)

shows a homogenous cobalt and indium distribution. Transmission electron microscopy (TEM) displays irregularly shaped, crystalline nanoparticles with diameters of around 20–100 nm. Inductively coupled plasma optical emission spectroscopy (ICP-OES, Figure 2a inset) reveals that the cobalt-to-indium ratio is only one-to-two instead of the expected one-to-three.

To understand the mismatch in the cobalt-to-indium ratio structurally, we collected cobalt K-edge X-ray absorption spectroscopy (XAS) data. The X-ray absorption near edge structure (XANES, Figure S2, Supporting Information) of cobalt indium nanoparticles shows a shape that resembles cobalt metal with a typical shallow edge rise, as expected for an intermetallic compound. Simulation of the extended X-ray absorption fine structure (EXAFS, Figure S3a–c, Supporting Information) spectrum of cobalt/indium reveals less than seven Co–In distances of ≈ 2.65 Å per cobalt center. For a good EXAFS simulation, a further cobalt–cobalt shell as characteristic for metallic cobalt at 2.45 Å was required because adding this interaction lowered the fit error from $\approx 20\%$ to 8% (Figure S3c, Supporting Information). In addition, the inclusion of cobalt–oxygen and cobalt–cobalt shells into the simulation of the spectrum of as-prepared cobalt indium, which may account for pre-oxidized cobalt sites, revealed only minor contributions from such species (Figure S3c, Supporting Information). We note here that the presence of multiple Co–Co and Co–In shells in the range of ≈ 2.45 –2.85 Å is expected to lead to spectral cancellation due to destructive interference of the respective EXAFS oscillations, which likely leads to underestimation of the Co coordination numbers. However, the trends in relative coordination numbers remain consistent. From the XAS data, we conclude that as-prepared cobalt indium nanoparticles contain crystalline, intermetallic CoIn_{3-x} , together with a cobalt richer phase. STEM-EDX mappings show that the sample does not contain pure cobalt but other cobalt indium phases, of which a cobalt-to-indium ratio of 1 to 1.5 seems to be the lower limit for the indium content (Figure S4, Supporting Information). Selected area diffraction (SAED) pattern measurements at various parts of the sample show a high crystallinity (Figure S5a, Supporting Information). Nevertheless, some particles contain amorphous shells (Figure S5b, Supporting Information). Due to the absence of reflexes not belonging to CoIn_3 in the XRD (Figure 2a), we reason that also these indium-deficient parts mostly crystallize in the CoIn_3 structure, while for very high cobalt contents amorphous phases form on the outside of the particles.

For comparison, EXAFS analysis of a pure cobalt powder sample showed that it was already partially oxidized, that is, as judged by approximately one oxygen bond per cobalt center (Figure S3c, Supporting Information) and shows a low degree of crystallinity, as indicated by the mere absence of second-shell Co–Co distances around 5–6 Å.

2.2. Electrocatalytic Activity toward the Oxygen Evolution Reaction

To investigate the electrocatalytic properties of cobalt indium nanoparticles in 1 M KOH (pH 13.89),^[32] we used a binder-free electrophoretic deposition approach (Figure S6, Supporting Information) on fluorine-doped tin oxide glass plate (FTO)

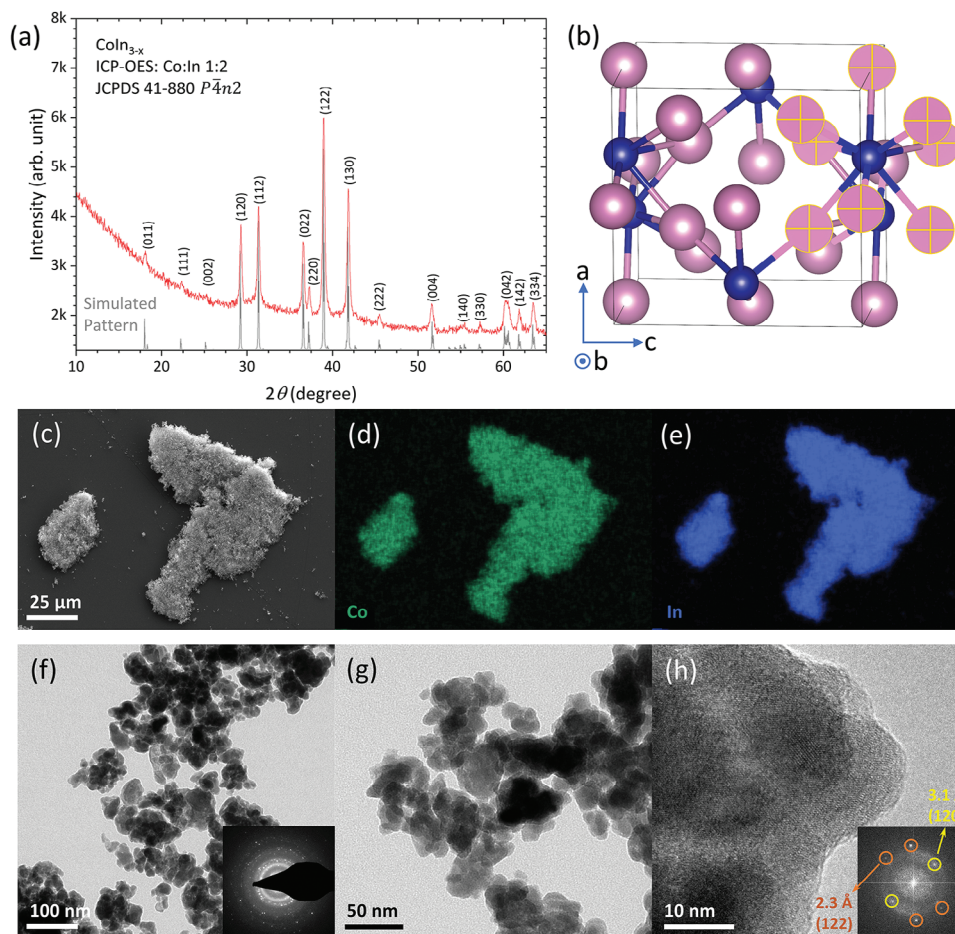


Figure 2. The as-prepared cobalt indium powder. a) XRD of cobalt indium with ICP-OES ratio and a simulated pattern using the unit cell shown in (b). b) The unit cell of CoIn_3 (ICPDS 41–880) with cobalt atoms in blue and indium in dark pink. Seven indium atoms surrounding one cobalt are marked with orange crosses to show the cobalt coordination. c–e) SEM-EDX elemental mapping. The respective EDX spectrum is shown in Figure S1, Supporting Information. f–h) TEM images showing the cobalt indium nanoparticles with a selected area diffraction pattern and a fast Fourier transform as insets in (f) and (h), respectively.

substrates. As reference materials, we synthesized pure cobalt nanoparticles (Figures S2 and S3 and S7–S9, Supporting Information) and pure indium (Figures S7 and S10, Supporting Information, for characterization) with the same wet chemical reduction approach used for cobalt indium. The pure indium shows no increased OER activity compared to bare FTO and thus is not further considered in depth. Double-layer capacitance measurements by cyclic voltammograms displayed no significant difference for metallic cobalt- and intermetallic cobalt-indium-loaded FTOs (Figures S11 and S12, Supporting Information). Before further electrocatalytic measurements were performed, the electrodes were activated in a chronoamperometry (CA) measurement at 1.72 V versus a reversible hydrogen electrode (V_{RHE}) for 90 min (Figure 3a). After this activation, cyclic voltammetry displays overpotentials at 10 mA cm^{-2} of 370 ± 9 and 420 ± 8 mV for cobalt indium and cobalt, respectively (Figure 3b, left y-axis, solid lines, errors from the standard deviation of three independent measurements). A magnification and discussion of the redox peak region is shown in Figure S13, Supporting Information. We note here that the total mass loading of both samples was

kept around $200 \mu\text{g cm}^{-2}$. Since cobalt indium contains only 20% cobalt, the activity difference between both samples per loaded cobalt is even larger (Figure 3b, right y-axis, dashed lines). Steady-state Tafel analysis shows that the Tafel slopes of both cobalt-containing compounds are comparable (Figure 3c), indicating that they have the same kinds of active cobalt sites. After the initial activation and slight deactivation of the cobalt indium and cobalt electrode, respectively, the activity remains stable for the next 24 h (Figure 3d).

2.3. Post-Catalytic Diffraction and Electron Microscopy Analyses

The activation of the cobalt indium sample during the initial electrocatalytic activation (Figure 3a) indicates a structural change of the material. To investigate this change, we characterized the sample after this activation. XRD shows that some of the initial crystalline CoIn_3 phase remains (Figure S15, Supporting Information). Additionally, a peak consistent with $\text{In}(\text{OH})_3$ appears, which is the thermodynamic most stable indium phase under

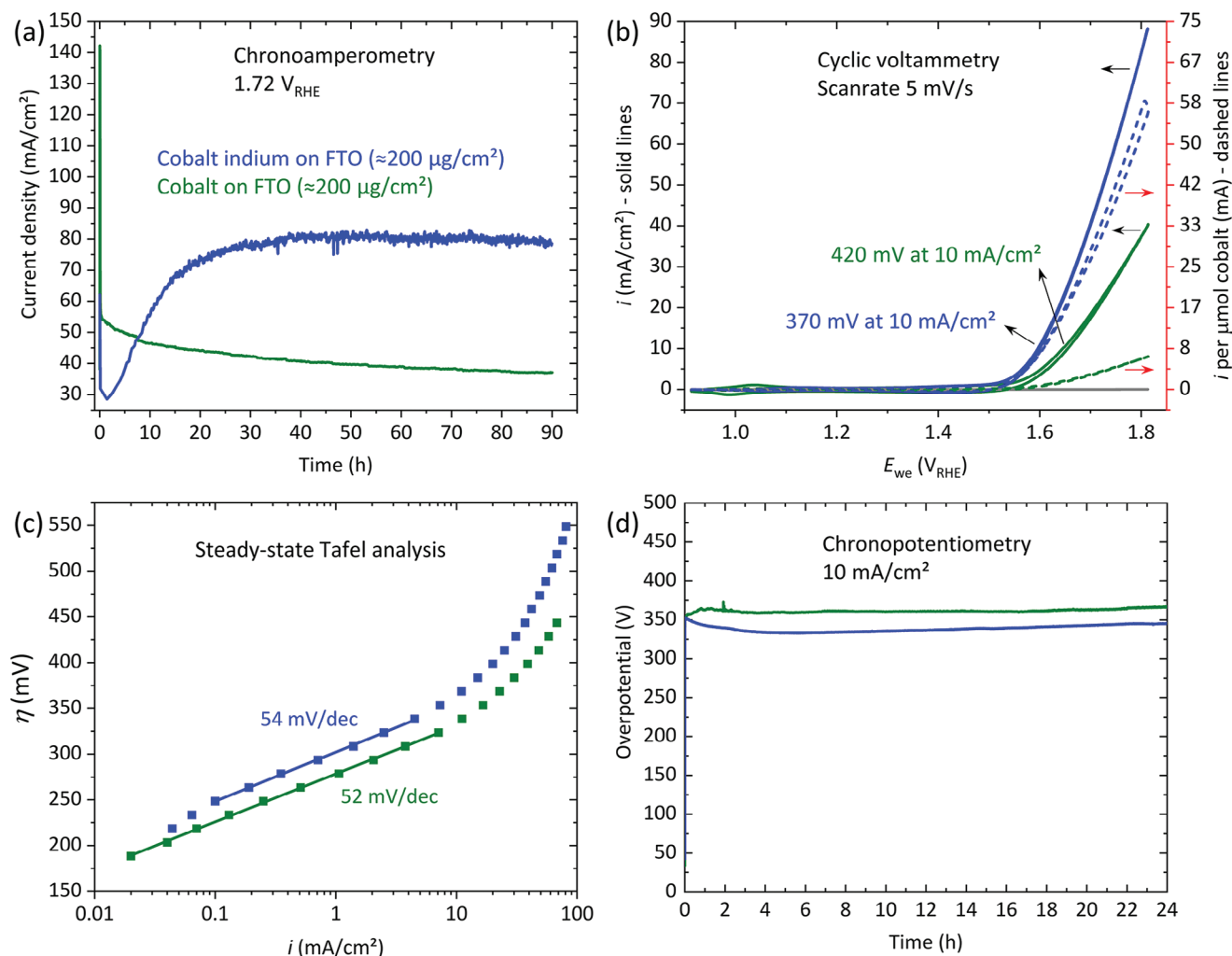


Figure 3. Electrochemical data of cobalt indium and cobalt nanoparticles on fluorine-doped tin oxide glass plates. Pure indium showed no OER activity. a) Activation of the as-deposited samples via chronoamperometry. The measurements of (b) and (c) were performed after this activation. b) Cyclic voltammograms normalized by current density (left y-axis, solid lines) and by the amount of cobalt loaded on the electrode (right y-axis, dashed lines). The grey line shows indium deposited on FTO. A magnification of the redox peak region is shown in Figure S13, Supporting Information. c) Tafel analysis obtained by 3-min chronoamperometry measurements (Figure S14, Supporting Information, for raw data). d) Chronopotentiometry measurements of the samples.

alkaline OER conditions (Figure 1 for Pourbaix diagram). SEM-EDX mappings cannot separate the cobalt indium and indium hydroxide phases (Figure S16, Supporting Information). Thus, we acquired a high-resolution scanning TEM mapping (Figure 4). This mapping shows the presence of three phases with different elemental distributions that we assign to indium hydroxide crystals, cobalt indium, and a phase containing mainly cobalt and oxygen. SAED patterns of the three different areas confirm the presence of the three respective phases (Figure S18, Supporting Information).

2.4. In Situ X-ray Absorption Spectroscopy

To gain more information about the structure of the intermetallic cobalt indium and metallic cobalt electrode during the OER, we freeze-quenched samples in liquid nitrogen after being op-

erated for 90 min at 1.72 V_{RHE} and measured cobalt K-edge XAS. The estimated quasi-in-situ cobalt oxidation state was 2.8 (Figure 5a for XANES and Figure S19, Supporting Information, for oxidation state determination), showing that mostly cobalt(III) species were present. The EXAFS (Figure 5b) was simulated using three shells (Figure 5c and Figure S15c, Supporting Information): a Co–O and a Co–Co shell accounting for layered cobalt-oxyhydroxide, as well as a Co–In shell reflecting remaining as-prepared material. In a fully ordered oxyhydroxide, the coordination number (N) of Co–O bonds at ≈ 1.9 Å should be close to six for mainly octahedral sites. The N -value of such a Co–O shell was only ≈ 0.6 in the as-prepared cobalt indium material, reflecting minor (surface) pre-oxidation. After 90 min at 1.72 V_{RHE} (Figure 3a), the N -value of this shell largely increased to ≈ 4.6 , revealing that most of the material (around 75%) reconstructed into cobalt oxyhydroxide. The residual cobalt remains in the original cobalt indium structure, consistent with the

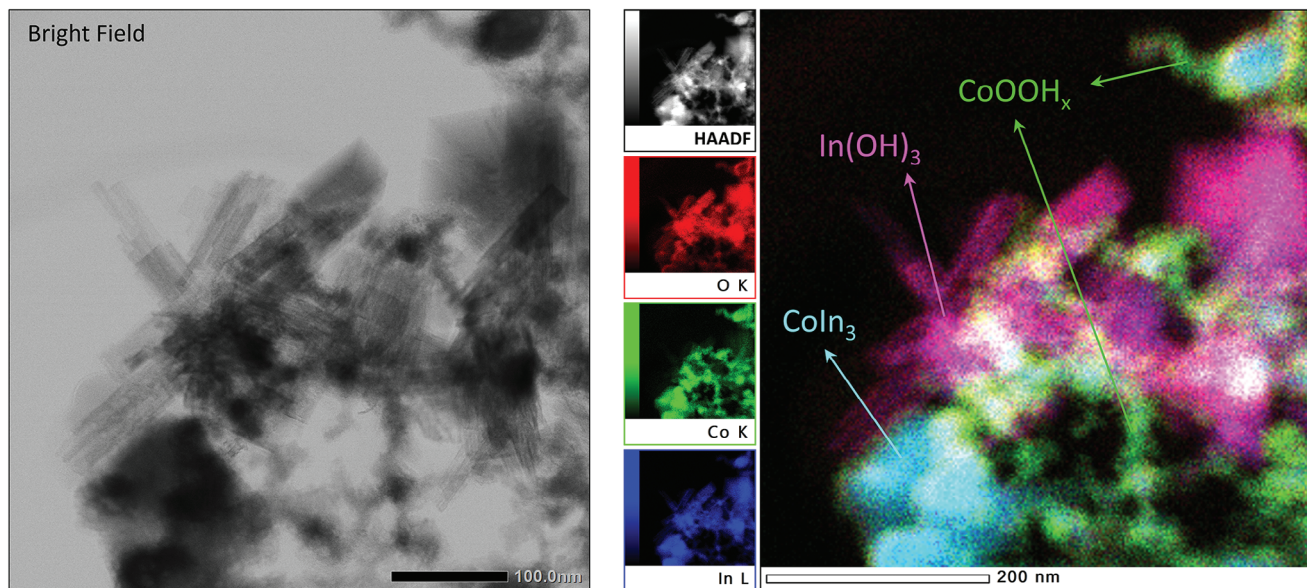


Figure 4. High-resolution STEM-EDX mapping of cobalt indium after 90 min at 1.72 V_{RHE} (Figure S17, Supporting Information, for EDX spectrum). This mapping shows the presence of three phases, one containing cobalt and oxygen, one containing indium and oxygen, and one containing cobalt and indium. Using SAED, XRD, and XAS, these three phases have been identified as $CoOOH_x$, $In(OH)_3$, and $CoIn_3$.

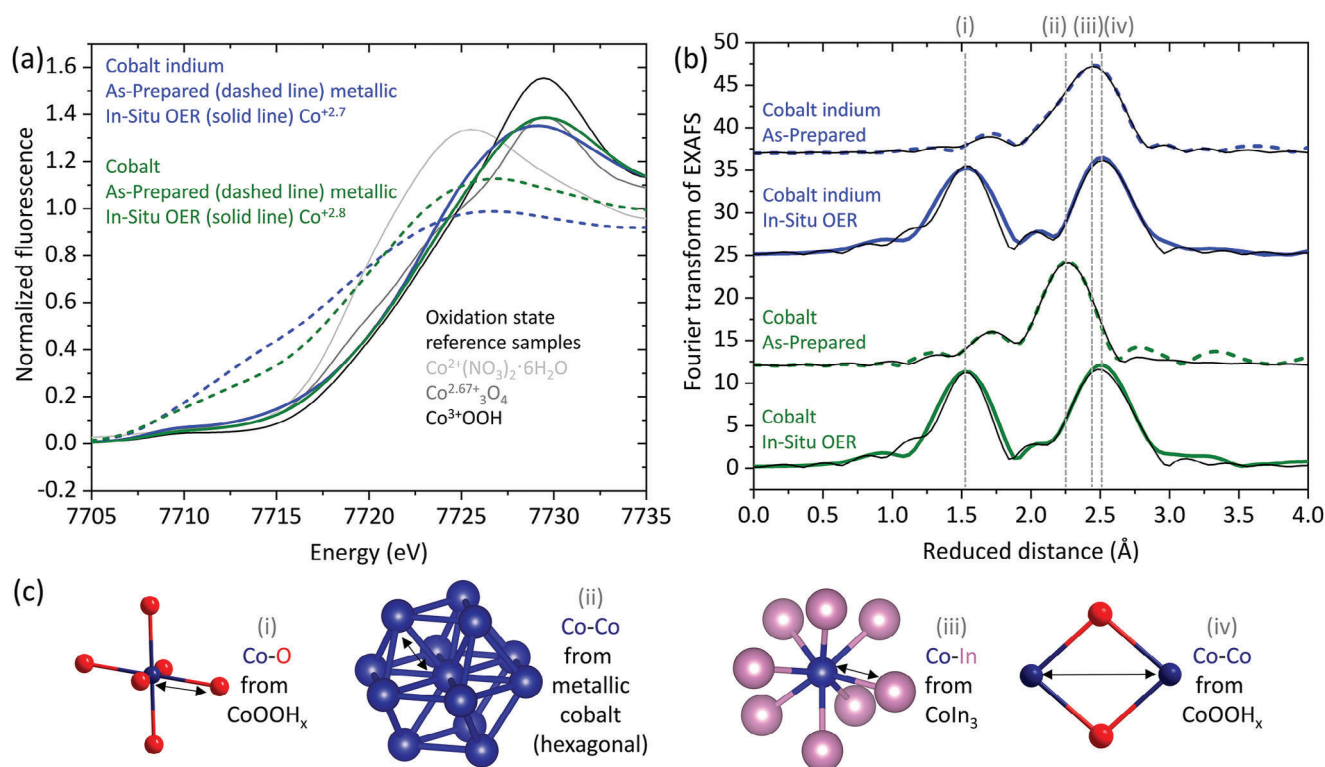


Figure 5. Cobalt K-edge X-ray absorption spectroscopy (XAS) data of cobalt indium and pure cobalt nanoparticles. As-prepared and quasi-in-situ (1.72 V_{RHE} for 90 min, Figure 2a) samples are compared. a) X-ray absorption near edge structure (XANES) spectra of cobalt indium and cobalt samples compared to spectra of cobalt +2, +2.67, and +3 references used for oxidation state determination (Figure S19, Supporting Information). b) Extended X-ray absorption fine structure (EXAFS) spectra (colored lines) and simulations (black lines). Further XAS data can be found in Figure S20, Supporting Information. The grey vertical dashes mark characteristic structural motifs of intermetallic cobalt indium (i), metallic cobalt (ii), and cobalt oxyhydroxide (i) and (ii). Respective structural motifs are shown in (c).

remaining Co–In shell population. The same analysis when performed for the pure cobalt nanoparticle reference sample (Figure 5 and Figure S15, Supporting Information) showed that this reference also reconstructs into cobalt oxyhydroxide to a similar extent as intermetallic cobalt indium.

3. Discussion

Cobalt indium nanoparticles (20–100 nm) have been prepared by a wet chemical approach and used as an OER catalyst on an inert FTO substrate. Cobalt nanoparticles, prepared by the same method, have been used as a reference. In situ and ex situ characterizations of both materials show that intermetallic cobalt indium and cobalt nanoparticles reconstruct into cobalt oxyhydroxides, as typical for cobalt-based precatalysts.^[19,33–35] Unlike other p-block elements, indium did not fully leach into the electrolyte as soluble oxyanions.^[15] Instead, a phase segregation occurred, wherein cobalt indium was reconstructed into cobalt oxyhydroxide and indium hydroxide. Thus, indium does not fully leach into the electrolyte and can remain at the electrode forming a solid heterostructure with the cobalt oxyhydroxide.

The cobalt oxyhydroxide phase formed from the cobalt indium precatalyst is more OER-active than the one formed from metallic cobalt. Cobalt indium activates and cobalt deactivates during the initial CA test (Figure 3a). Previously, it had been shown that the formation of separate, non-leaching phases (La(OH)₃ and NiOOH from LaNi₅) can provide a matrix that prevents the agglomeration of the active oxyhydroxides. This effect could explain the different long-term behavior of both samples.^[36,37] Tafel and local structural analysis (EXAFS) show that differences in the local cobalt environment, electronic structure, or kind of active sites do not cause this activity difference. Thus, it must originate from different numbers of available active sites in both materials. This phenomenon has previously been observed for cobalt oxyhydroxides formed from precursors with constituents that can leach during the OER.^[5,37] In such precatalysts, the leaching constituent takes the role of a sacrificial element, creating a high surface area and disordered active catalysts with more available active sites. The herein-revealed phase segregation of cobalt indium to cobalt oxyhydroxide and indium hydroxide also succeeds in exposing more active sites compared to a metallic cobalt precatalyst.

4. Conclusion

We have shown that cobalt indium prepared by a wet chemical approach reconstructs into a cobalt oxyhydroxide and indium hydroxide phase during the OER. The cobalt oxyhydroxide formed through this phase segregation process is more active than oxyhydroxides derived from cobalt metal nanoparticles due to more accessible active sites. Indium does mostly not leach into the electrolyte and remains at the active electrode. Therefore, this p-block element is suitable for forming heterostructured interfaces with other OER-active metal-oxo phases. Potentially, the herein observed phase segregation could be suitable for creating an interface between photoactive indium oxides and catalytically active cobalt oxyhydroxides. Most importantly, this work shows that not all p-block elements in OER precatalysts behave the same way, leaching to the electrolyte as oxyanions during operation. Thus,

investigating further novel phases containing transition metals and p-block elements may overcome the limitation of the design opportunities for OER catalysts caused by the reconstruction of merely all materials to similar oxyhydroxides.

Supporting Information

Supporting Information is available from the Wiley Online Library or from the author.

Acknowledgements

Funded by the German Federal Ministry of Education and Research in the framework of the project Catlab (03EW0015A/B) and project “Prometh2eus,” 03HY105C. STEM analysis was performed on a probe-corrected JEM-ARM300F2. The authors would also like to acknowledge the support from Deutsche Forschungsgemeinschaft (DFG, German Research Foundation) – GZ: INST 131/789-1 FUGG – 403371556 – and Germany’s Excellence Strategy – EXC 2008 – 390540038 – UniSysCat. X-ray absorption spectroscopy was performed at beamline KMC-3 of the BESSY synchrotron (Berlin-Adlershof) operated by the Helmholtz-Zentrum Berlin (HZB); The authors thank I. Zizak and G. Schuck for technical support.

Open access funding enabled and organized by Projekt DEAL.

Conflict of Interest

The authors declare no conflict of interest.

Data Availability Statement

The data that support the findings of this study are available from the corresponding author upon reasonable request.

Keywords

boron group 13 element, cobalt oxyhydroxide, in situ X-ray absorption spectroscopy, oxygen evolution reaction, reconstruction, water oxidation, water splitting

Received: October 26, 2023

Revised: February 3, 2024

Published online: February 17, 2024

- [1] R. Schlögl, *Angew. Chem., Int. Ed.* **2019**, *58*, 343.
- [2] T. Kahlstorf, J. N. Hausmann, T. Sontheimer, P. W. Menezes, *Global Challenges* **2023**, *7*, 2200242.
- [3] Z. Wu, X. F. Lu, S. Zang, X. W. (David) Lou, *Adv. Funct. Mater.* **2020**, *30*, 1910274.
- [4] W. Li, D. Xiong, X. Gao, L. Liu, *Chem. Commun.* **2019**, *55*, 8744.
- [5] J. N. Hausmann, P. W. Menezes, *Curr. Opin. Electrochem.* **2022**, *34*, 100991.
- [6] J. N. Hausmann, E. M. Heppke, R. Beltrán-Suito, J. Schmidt, M. Mühlbauer, M. Lerch, P. W. Menezes, M. Driess, *ChemCatChem* **2020**, *12*, 1161.
- [7] B. Dasgupta, J. N. Hausmann, R. Beltrán-Suito, S. Kalra, K. Laun, I. Zebger, M. Driess, P. W. Menezes, *Small* **2023**, *19*, 2301258.
- [8] M. W. Kanan, D. G. Nocera, *Science* **2008**, *321*, 1072.

- [9] L. Reith, J. N. Hausmann, S. Mebs, I. Mondal, H. Dau, M. Driess, P. W. Menezes, *Adv. Energy Mater.* **2023**, *13*, 2203886.
- [10] J. N. Hausmann, S. Mebs, H. Dau, M. Driess, P. W. Menezes, *Adv. Mater.* **2022**, *34*, 2207494.
- [11] J. Masa, P. Weide, D. Peeters, I. Sinev, W. Xia, Z. Sun, C. Somsen, M. Muhler, W. Schuhmann, *Adv. Energy Mater.* **2016**, *6*, 1502313.
- [12] J. N. Hausmann, R. A. Khalaniya, C. Das, I. Remy-Speckmann, S. Berendts, A. V. Shevelkov, M. Driess, P. W. Menezes, *Chem. Commun.* **2021**, *57*, 2184.
- [13] J. N. Hausmann, R. Beltrán-Suito, S. Mebs, V. Hlukhyy, T. F. Fässler, H. Dau, M. Driess, P. W. Menezes, *Adv. Mater.* **2021**, *33*, 2008823.
- [14] J. Masa, W. Schuhmann, *ChemCatChem* **2019**, *11*, 5842.
- [15] J. N. W. Hausmann, P. W. Menezes, *Angew. Chem., Int. Ed.* **2022**, *61*, 202207279.
- [16] Y. Li, X. Du, J. Huang, C. Wu, Y. Sun, G. Zou, C. Yang, J. Xiong, *Small* **2019**, *15*, 1901980.
- [17] X. Liu, J. Meng, J. Zhu, M. Huang, B. Wen, R. Guo, L. Mai, *Adv. Mater.* **2021**, *33*, 2007344.
- [18] A. Sivanantham, P. Ganesan, A. Vinu, S. Shanmugam, *ACS Catal.* **2020**, *10*, 463.
- [19] B. R. Wygant, K. Kawashima, C. B. Mullins, *ACS Energy Lett.* **2018**, *3*, 2956.
- [20] G. K. Schweitzer, L. L. Pesterfield, *The Aqueous Chemistry of the Elements*, Oxford University Press, Oxford **2010**.
- [21] J. Wang, X. Zheng, Y. Cao, L. Li, C. Zhong, Y. Deng, X. Han, W. Hu, *ACS Appl. Mater. Interfaces* **2020**, *12*, 8115.
- [22] J. Han, Q. Wei, J. Zhang, B. Zhang, C. Li, W. Wang, L. Cao, B. Dong, *J. Mater. Chem. A* **2020**, *8*, 18232.
- [23] G. Fu, Y. Wang, Y. Tang, K. Zhou, J. B. Goodenough, J. M. Lee, *ACS Mater. Lett.* **2019**, *1*, 123.
- [24] N. Lethukuthula, M. D. Khan, S. C. Masikane, F. M. De Souza, J. Choi, R. K. Gupta, N. Revaprasadu, *Mater. Sci. Semicond. Process.* **2023**, *156*, 107252.
- [25] X. Chen, H. Zhu, J. Zhu, H. Zhang, *Chem. Eng. J.* **2023**, *451*, 138998.
- [26] S. Chen, C. Wang, F. Gao, Y. Yang, M. Huang, H. Tong, Z. Cheng, P. Wang, P. Wang, J. Tu, X. Zeng, Q. Chen, *J. Mater. Chem. A* **2022**, *10*, 3722.
- [27] U. Shamraiz, Elizbit, A. B., A. Alfantazi, H. Hussain, B. Raza, S. Ullah, I. R. Green, *J. Electrochem. Soc.* **2021**, *168*, 066510.
- [28] L. Yang, J. Han, J. Zhang, Y. Li, W. Wang, L. Cao, B. Dong, *ChemElectroChem* **2020**, *7*, 3991.
- [29] X. Gan, R. Zheng, T. Liu, J. Meng, R. Chen, X. Sun, X. Sun, *Chemistry* **2017**, *23*, 7264.
- [30] M. Meng, X. Wu, X. Zhu, L. Yang, Z. Gan, X. Zhu, L. Liu, P. K. Chu, *J. Phys. Chem. Lett.* **2014**, *5*, 4298.
- [31] M. Metikoš-Huković, S. Omanović, *J. Electroanal. Chem.* **1998**, *455*, 181.
- [32] J. N. Hausmann, B. Traynor, R. J. Myers, M. Driess, P. W. Menezes, *ACS Energy Lett.* **2021**, *6*, 3567.
- [33] J. N. Hausmann, S. Mebs, K. Laun, I. Zebger, H. Dau, P. W. Menezes, M. Driess, *Energy Environ. Sci.* **2020**, *13*, 3607.
- [34] S. W. Lee, C. Carlton, M. Risch, Y. Surendranath, S. Chen, S. Furutsuki, A. Yamada, D. G. Nocera, Y. Shao-Horn, *J. Am. Chem. Soc.* **2012**, *134*, 16959.
- [35] B. S. Yeo, A. T. Bell, *J. Am. Chem. Soc.* **2011**, *133*, 5587.
- [36] Z. Chen, H. Yang, S. Mebs, H. Dau, M. Driess, Z. Wang, Z. Kang, P. W. Menezes, *Adv. Mater.* **2023**, *35*, 2208337.
- [37] Z. Chen, H. Yang, Z. Kang, M. Driess, P. W. Menezes, *Adv. Mater.* **2022**, *34*, 2108432.